Supporting Information

Photochemical Activated Atomic Ruthenium Supported on Boron-Doped Carbon as a Robust Electrocatalyst for Hydrogen Evolution

Yihuan Yu, Shaoxuan Yang, Meiling Dou, Zhengping Zhang [a,b] *, Feng Wang* [a,b] *

[a] State Key Laboratory of Chemical Resource Engineering, Beijing Key Laboratory of Electrochemical Process and Technology for Materials, Beijing University of Chemical Technology, Beijing 100029, P. R. China

[b] Beijing Advanced Innovation Center for Soft Matter Science and Engineering, Beijing University of Chemical Technology, Beijing 100029, P. R. China

E-mail: wangf@mail.buct.edu.cn; zhangzhengping@mail.buct.edu.cn

Experimental Methods

Materials. Boric acid, phenol, ethanol, formaldehyde (37 wt.%), sodium hydroxide (NaOH), hydrochloric acid (HCl ~35%), urea, isopropanol, ruthenium trichloride and commercial RuO_2 were purchased from Sinopharm. High purity argon and nitrogen gas were bought from Beijing AP BAIF Gases Industry Co. Ltd. Pluronic F127, Commercial Ru/C (5 wt.%), Commercial Pt/C (20 wt.%), and Nafion solution (5 wt.%) were purchased from Sigma-Aldrich, Johnson Matthey and DuPont, respectively. Ultrapure water (18.2 MΩ cm) obtained from a water purification system (TTL-6B) without further purity.

Material Characterization. Powder X-ray diffraction (XRD) patterns were profiled on a X-ray diffractometer (D/max-2500, Rigaku, Japan) with Cu Kα radiation (λ = 1.54056 Å) source. Scanning electron microscopy (SEM) and high-resolution transmission electron microscopy (HR-TEM) images were taken on the FE-JSM-6701F (JEOL, Japan) and JSM-2100 (JEOL, Japan) microscopes, respectively. The high-angle annular dark-field and annular bright-field scanning transmission electron microscope (HADDF-STEM, ABF-STEM) images were taken on JEM-ARM200F. The Brunauer-Emmett-Teller (BET) specific surface area and pore size distribution were determined by nitrogen adsorption-desorption measurements with a Quantachrome AUTOSORB-SI instrument. Raman spectra were recorded with a Horiba Jobin Yvon LabRam HR800 confocal microscope using a laser of 632.8 nm. The X-ray photoelectron spectroscopy (XPS) was performed with the Thermo Fisher Scientific ESCALAB 250 spectrometer using the C 1s peak (285 eV) as the reference for binding energy calibration. The actual Ru content was measured by inductively coupled plasma atomic emission spectroscopy (ICP-AES) was performed by (7700, Agilent Technologies Inc., U.S.A.).

Electrochemical Measurements. All the electrochemical measurements were conducted with a standard three electrode system controlled by a CHI 760E electrochemistry workstation. Catalyst powders cast on the L-type glassy carbon electrode was used as work electrode, commercial dimensionally stable anode (DSA) was used as the counter electrode and saturated calomel electrode as the reference electrode. The reference electrode was calibrated against and converted to reversible hydrogen electrode (RHE). Linear sweep voltammetry (LSV) was carried out at 5 mV/s for the polarization curves. The hybrid catalyst was cycled ~40 times by cyclic voltammetry (CV) until a stable CV curve was developed before measuring polarization curves of samples. All polarization curves were compensated with 100% *iR*-compensation. Electrochemical impedance spectroscopy (EIS) measurements were carried out from 100 kHz to 0.1 Hz with an amplitude of 5 mV at open-circuit voltage. The Faraday efficiency experiments involving rotating ring disk electrode (RRDE) were conducted with CHI 760E electrochemistry workstation using a standard three-electrode system at room temperature. A glassy carbon RRDE coated with electrocatalyst was used as the working electrode, a graphite rod and a saturated calomel electrode as the counter and reference electrodes, respectively. The working electrode continuously rotating at 1600 rpm to get rid of the hydrogen bubbles and the collection efficiency (N) of ring electrode is 0.37. All potentials reported in this work were in reference to the reversible hydrogen electrode (RHE). In a typical preparation of working electrode, 10 mg of electrocatalyst was ultrasonically blending with 2.0 mL of ethanol and 20 μL of Nafion (5 wt.%, Dupont) for 0.5 h to form a homogeneous electrocatalyst ink, 10 μL of which was transferred onto the L-type glassy carbon electrode or RRDE, leading to a geometric loading of 0.394 mg cm^{-2}. The commercial Pt/C (20 wt.% of Pt, Johnson Matthey) working electrode was also used as a reference with the Pt loading of 20 μg cm^{-2}. All the potentials were calibrated to

the potentials vs. RHE (Potentials vs. RHE = potential vs. SCE + 0.241 + 0.0591 * pH V). The ORR

experiments were carried out in 1 M KOH or 0.5 M H_2SO_4 solution at the ambient temperature after

being purged with N_2 gas for 20 min. The L-type glassy carbon electrode and glassy carbon rotating

disk electrode are both 4 mm in diameter.

For the Turnover Frequency (TOF) calculation of the catalysts, The TOF value is calculated

from the equation:

$$TOF = \frac{I}{2Fn}$$

where I is the current (A) during linear sweep measurement, F is the Faraday constant (C/mol),

n is the number of metal amount (mol). The factor 1/2 is based on the consideration that two

electrons are required to form one hydrogen molecule.

Computational Approach. The density functional theory (DFT) calculations were conducted

by the program DMol3 Materials Studio (Accelrys Inc.) with Perdew-Burke-Ernzerhof generalized

gradient approximation (PBE-GGA) correlation functional. Spin-unrestricted has also been

considered in our calculation when it is necessary. For all theoretical models, the convergence

threshold was set as 10^{-5} eV in energy. The adsorption free energy of atomic hydrogen

(ΔG_{H*}) was calculated by the equation $\Delta G_{H*} = \Delta E_{H*} + \Delta ZPE - T\Delta S$, where ΔE_{H*} is the

differential hydrogen adsorption energy, ΔZPE is the difference in zero point energy

between the adsorbed hydrogen and hydrogen in the gas phase and ΔS is the entropy

difference between the adsorbed state and the gas phase. The contribution from the

configurational entropy in the adsorbed state is small and is neglected. We can take the

entropy of hydrogen adsorption as $\Delta S = 1/2 \ S_{H2}$ where S_{H2} is the entropy of molecule

hydrogen in the gas phase at standard conditions. In this work, the ΔZPE and $T\Delta S$ were

computed by following the scheme proposed by Nørskov et al.

Supporting Results and Discussion.

Table S1. Pore characteristics of MCS, BMCS, Ru–N/BC, Ru/BC, Ru–N/C and Ru/C.

sample	S_{BET} $(m^2\,g^{-1})$	S_{micro} $(m^2\,g^{-1})$	S_{meso} $(m^2\,g^{-1})$	Volume $(cm^3\,g^{-1})$	V_{micro} $(cm^3\,g^{-1})$	V_{meso} $(cm^3\,g^{-1})$
BMCS	953	496	457	0.696	0.206	0.490
Ru/BC	899	480	419	0.647	0.199	0.448
Ru–N/BC	803	415	388	0.545	0.173	0.372
MCS	869	594	275	0.506	0.258	0.248
Ru/C	745	578	167	0.414	0.241	0.173
Ru–N/C	697	577	120	0.373	0.229	0.144

Table S2. The Ru content of Ru/C, Ru–N/C, Ru/BC, Ru–N/BC measured by inductively coupled plasma atomic emission spectroscopy (ICP-AES).

sample	wt.%
Ru/C	0.56%
Ru–N/C	0.54%
Ru/BC	0.45%
Ru–N/BC	0.46%
Ru–N/BC-after*	0.41%

* Ru–N/BC-after chronopotentiometry tests in 0.5 M H_2SO_4 solution.

Table S3. The C-, N-, O-, B- and Ru-content of BMCS, Ru/BC, Ru–N/BC, MCS, Ru/C and Ru–N/C.

Sample	C (at.%)	O (at.%)	B (at.%) total	B-N	BC_2O	BCO_2	Ru (at.%)	N (at.%) Total	Pyridinic	C-N-B	pyrrolic	quaternary
BMCS	87.48	10.73	1.79	-	67.89%	32.11%	-	-	-	-	-	-
Ru/BC	83.89	15.32	1.87	-	62.76%	37.24%-	0.32	-	-	-	-	-
Ru–N/BC	84.85	11.93	1.39	20.44%	55.16%	24.40%	0.54	1.29	23.84%	21.28%	21.54%	33.34%
MCS	92.11	7.89	-	-	-	-	-	-	-	-	-	-
Ru/C	81.83	17.35	-	-	-	-	0.82	-	-	-	-	-
Ru–N/C	84.83	12.59	-	-	-	-	0.91	1.67	14.02%	-	42.99%	42.99%

Table S4. The fitting Parameters of EXAFS fits for the Ru/C, Ru–N/C, Ru/BC and Ru–N/BC.

Samples	First shell path	Coordination number*	Bond length Reff (Å)	Bond length R (Å)	R factor (%)
Ru/C	Ru-C	3	2.08	1.53	0.002
Ru–N/C	Ru–N(C)	3	2.02	1.50	0.005
Ru/BC	Ru-C	3	2.08	1.56	0.010
Ru–N/BC	Ru–N(C)	3	1.76	1.38	0.012

*The coordination number was fixed during the fitting.

Table S5. Constraint parameters during the DFT geometry optimization.

Samples	ΔE (Ha*)	$|F|_{max}$ (Ha Å^{-1})	$|dR|_{max}$ (Å)
Ru/C	-0.0000199	0.000849	0.003554
Ru–N/C	-0.0000099	0.000482	0.004375
Ru/BC	-0.0000083	0.000501	0.002428
Ru–N/BC	-0.0000198	0.000731	0.004635

Ha* = 27.21 eV, the same below

Table S6. Calculated results of corresponding energy by using DFT method.

sample	$E_{support}$/Ha	E_{metal}/Ha	$E_{electrocatalyst}$/Ha	ΔE_{rem}*/Ha	ΔE_{rem}/eV
Ru–N/BC	-1810.57	-4441.27	-6252.01	0.17	4.62
Ru/BC	-1776.83	-4441.27	-6218.19	0.08	2.18
Ru–N/C	-1823.45	-4441.27	-6264.81	0.09	2.45
Ru/C	-1790.56	-4441.27	-6231.86	0.03	0.82

ΔE_{rem}* = $E_{support}$ + E_{metal} - $E_{electrocatalyst}$

Table S7. Electrochemical impedance spectroscopy (EIS) measurement of Ru/BC, Ru–N/BC, Ru–N/C, Ru/C, commercial RuO_2, commercial Ru/C (5 wt.%) and commercial Pt/C (20 wt.%).

Sample	R_s (Ohm)		R_{ct} (Ohm)	
	1M KOH	0.5M H_2SO_4	1M KOH	0.5M H_2SO_4
Ru–N/BC	7.2	12.5	20.3	32.6
Ru/BC	7.4	12.6	55.1	60.6
Ru–N/C	7.9	8.5	107.4	150.0
Ru/C	8.6	8.8	203.0	291.5
commercial RuO_2	9.7	11.1	76.5	262.9
commercial Ru/C (5 wt.%)	8.6	15.8	45.6	68.6
commercial Pt/C (20 wt.%)	9.3	7.9	47.6	15.9

Table S8. The electrochemical performance of Ru/BC, Ru–N/BC, Ru–N/C, Ru/C, commercial RuO$_2$, commercial Ru/C (5 wt.%) and commercial Pt/C (20 wt.%). in 1 M KOH

Sample	η @ 10mA cm^{-2} (mV)	j$_0$* (mA cm^{-2})	Mass activity @ -0.100 V* (mA ug^{-1}$_{metal}$)
Ru–N/BC	51	0.78	19.56
Ru/BC	73	0.52	11.36
Ru–N/C	98	0.45	5.79
Ru/C	100	0.39	3.39
commercial Ru/C (5 wt.%)	82	0.63	0.53
commercial Pt/C (20 wt.%)	64	0.21	0.60

V*: versus reversible hydrogen electrode, vs. RHE, the same below

j$_0$*: Exchange current density, the same below

Table S9. The electrochemical performance of Ru/BC, Ru–N/BC, Ru–N/C, Ru/C, commercial RuO$_2$, commercial Ru/C (5 wt.%) and commercial Pt/C (20 wt.%). in 0.5 M H$_2$SO$_4$

Sample	η @ 10mA cm^{-2} (mV)	j$_0$* (mA cm^{-2})	Mass activity @ -0.1 V* (mA ug^{-1}$_{metal}$)
Ru–N/BC	79	0.51	10.38
Ru/BC	116	0.35	3.32
Ru–N/C	134	0.17	1.65
Ru/C	148	0.14	1.22
commercial Ru/C (5 wt.%)	97	0.09	0.72
commercial Pt/C (20 wt.%)	27	1.04	2.01
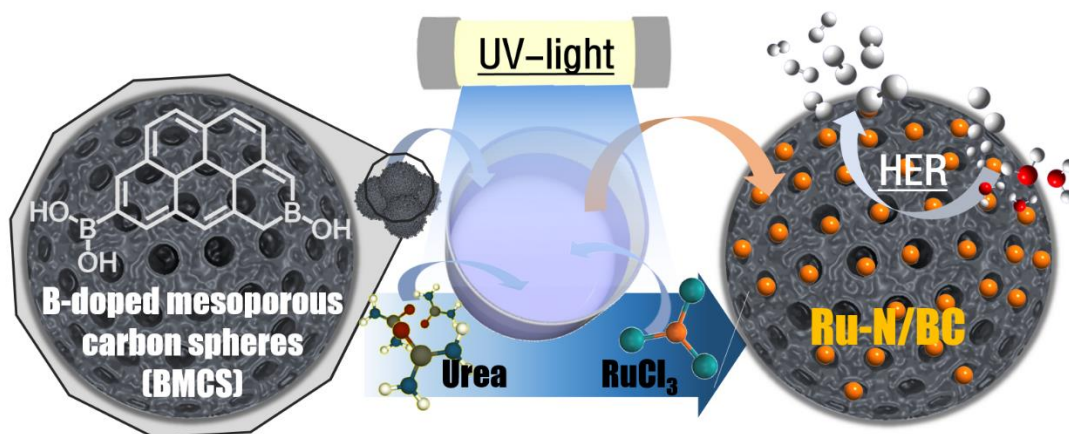
Scheme S1. The Schematic illustration of the synthesis of the Ru–N/BC electrocatalyst.
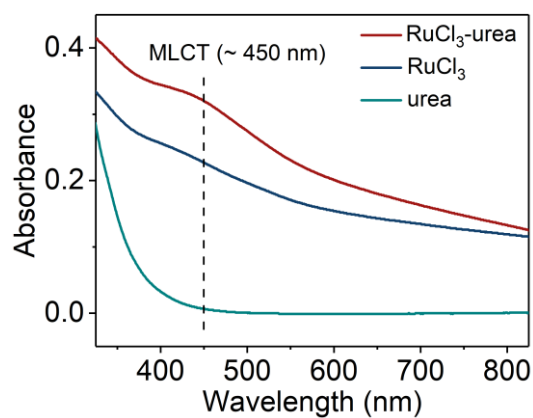
Figure S1. UV-Vis spectroscopy of $RuCl_3$, urea and $RuCl_3$-urea complex.
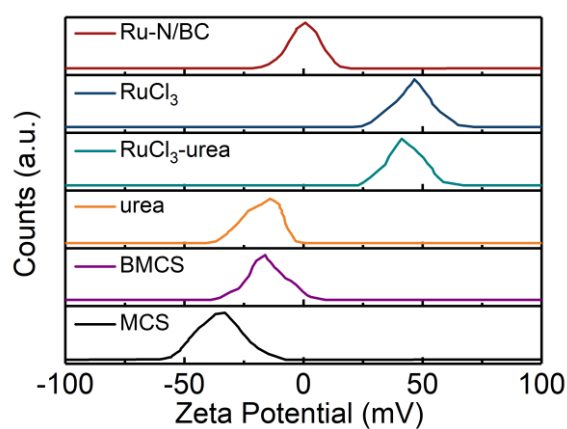
Figure S2. Zeta Potential of Ru–N/BC, $RuCl_3$, urea, $RuCl_3$–urea complex, BMCS and MCS.
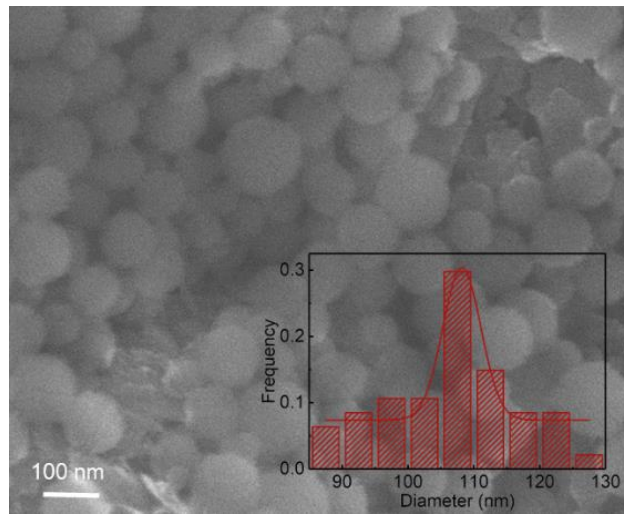
Figure S3. SEM image of resin spheres.
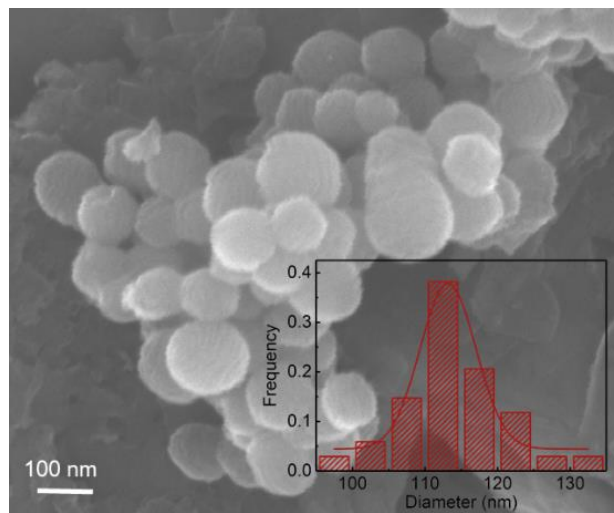
Figure S4. SEM image of BMCS.
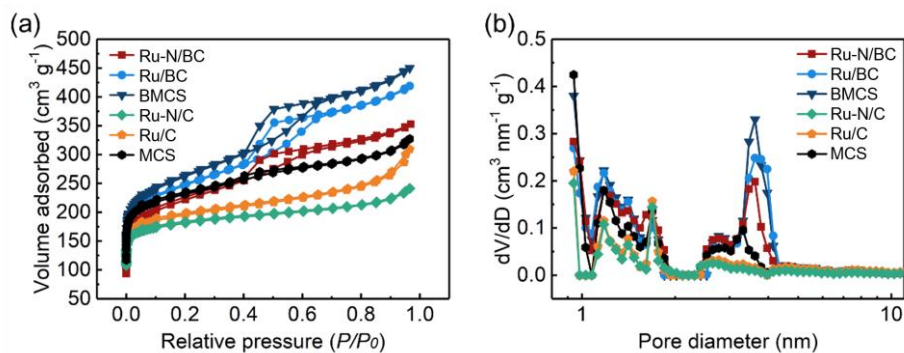
Figure S5. (a) N_2 adsorption/desorption isotherms of Ru–N/BC, Ru/BC, BMCS, Ru–N/C, Ru/C and MCS and (b) corresponding pore size distribution plots.
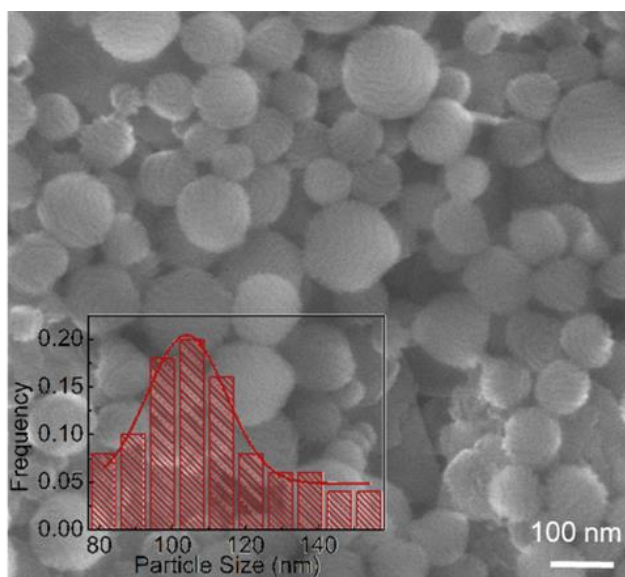
Figure S6. SEM image of Ru–N/BC.
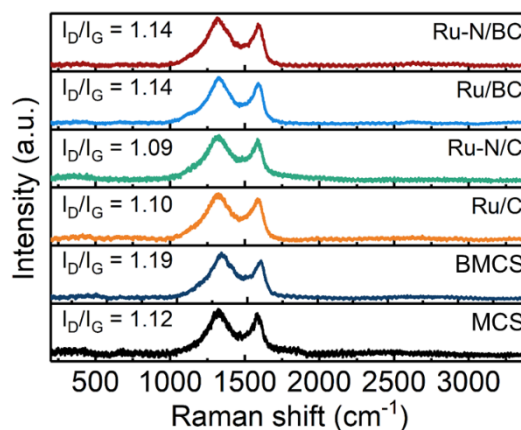
Figure S7. Raman spectra of Ru–N/BC, Ru/BC, Ru–N/C, Ru/C, BMCS and MCS.
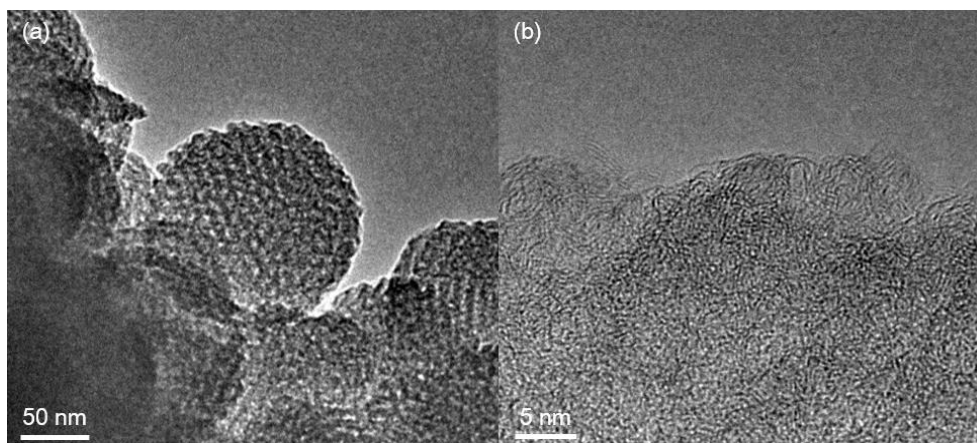
Figure S8. (a) TEM image of BMCS and (b) HR-TEM image of BMCS.
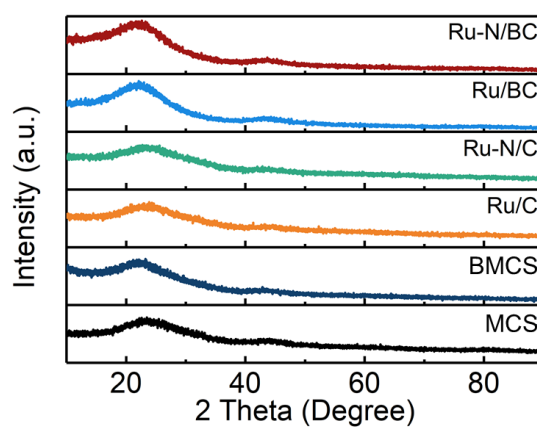
Figure S9. XRD patterns of Ru–N/BC, Ru/BC, Ru–N/C, Ru/C, BMCS and MCS.
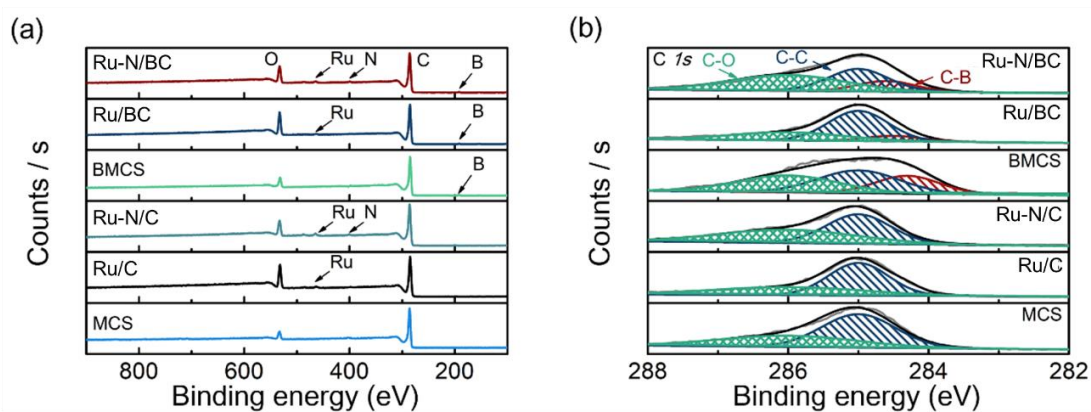
Figure S10. (a) The XPS survey spectra and (b) High-resolution XPS spectra of C 1s for Ru–

N/BC, Ru/BC, BMCS, Ru–N/C, Ru/C and MCS.
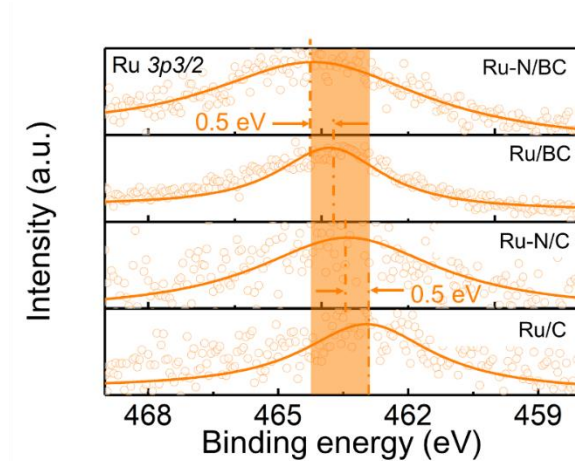
Figure S11. High-resolution XPS spectra of Ru 3*p* for Ru–N/BC, Ru/BC, Ru–N/C and Ru/C.
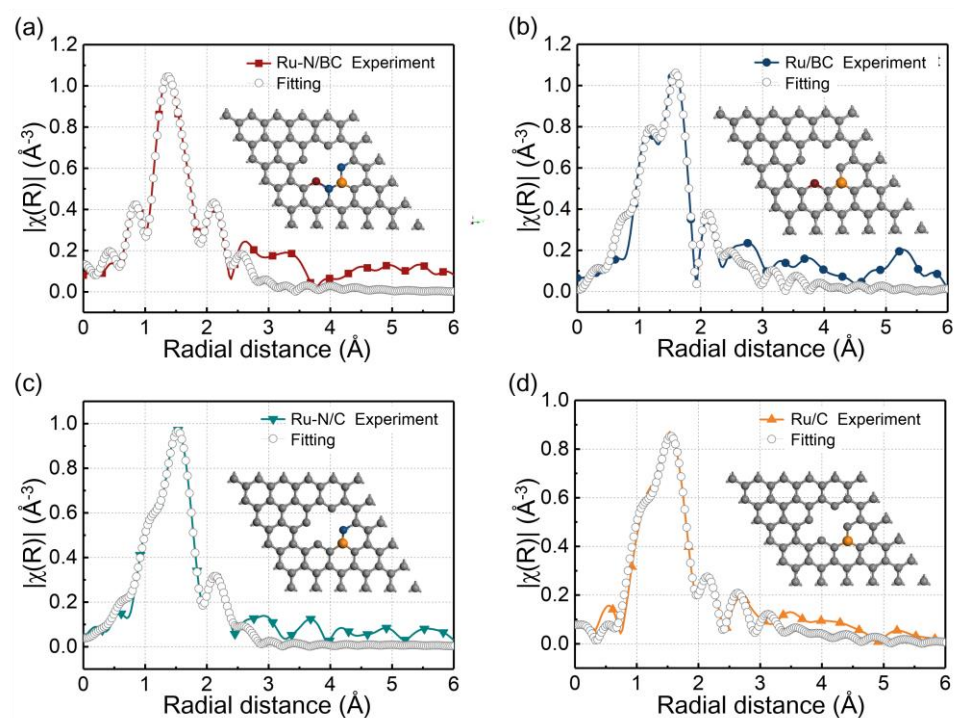
Figure S12. Comparison between the experimental EXAFS spectra of (a) Ru–N/BC, (b) Ru/BC,

(c) Ru–N/C, and (d) Ru/C and the theoretical spectrum calculated from the depicted structures

(inset)
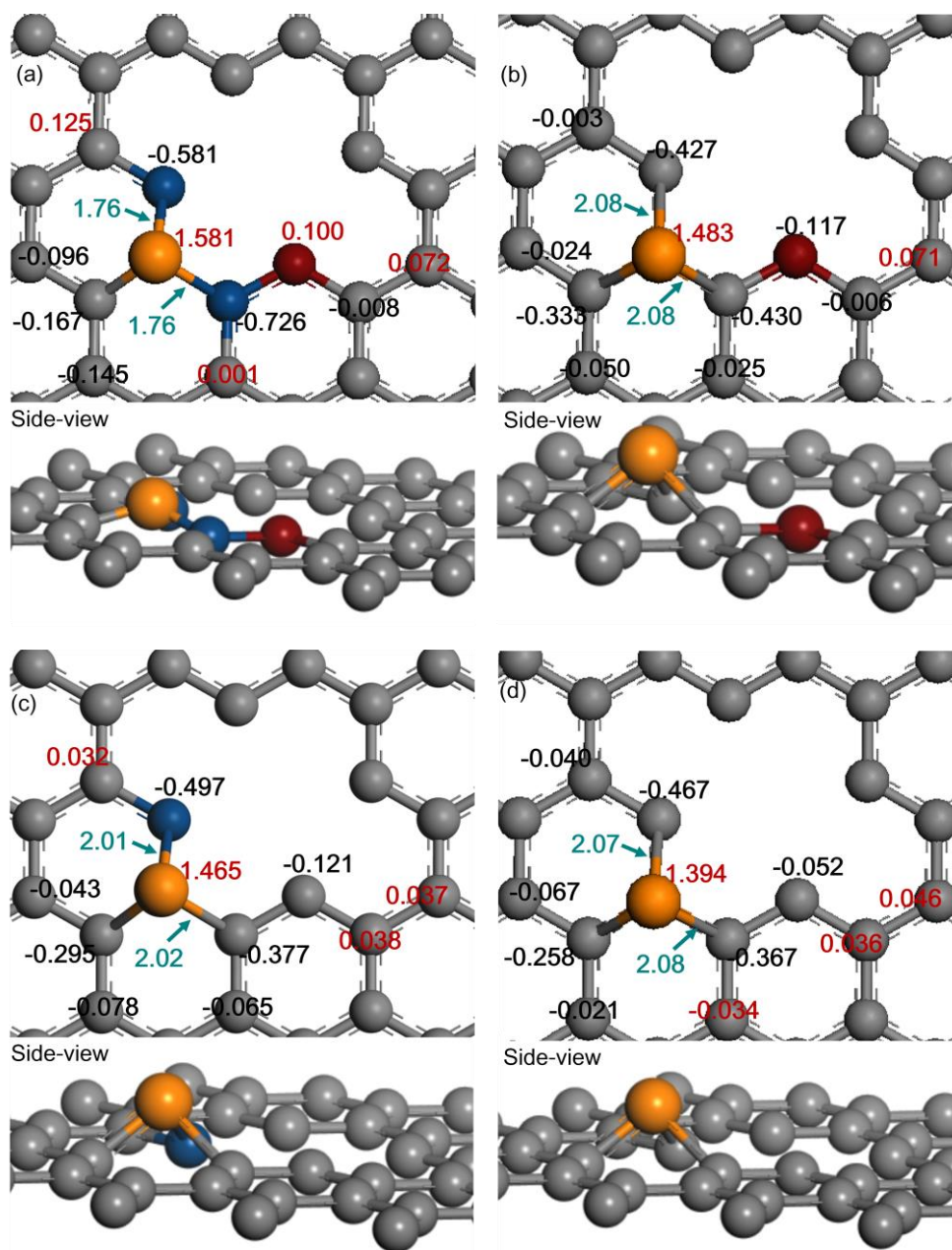
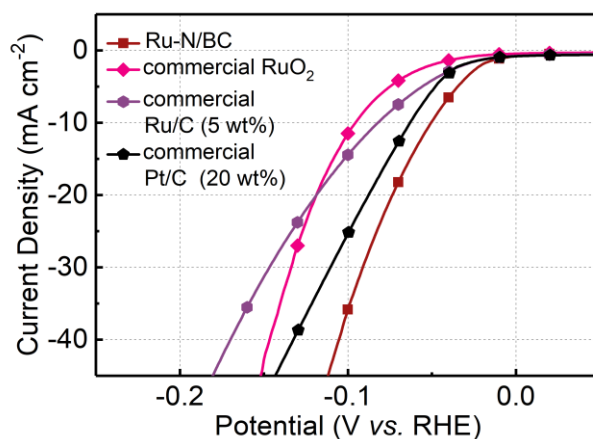**Figure S13.** Charge distribution of the depicted structures of (a) Ru/BC, (b) Ru–N/C, (c) Ru/C and (d) Ru–N/BC

Figure S14. LSV plots of the Ru–N/BC, commercial RuO_2, commercial Ru/C (5 wt.%) and commercial Pt/C (20 wt.%) electrodes in N_2-saturated 1 M KOH solution at a sweep rate of 5 mV s^{-1}.
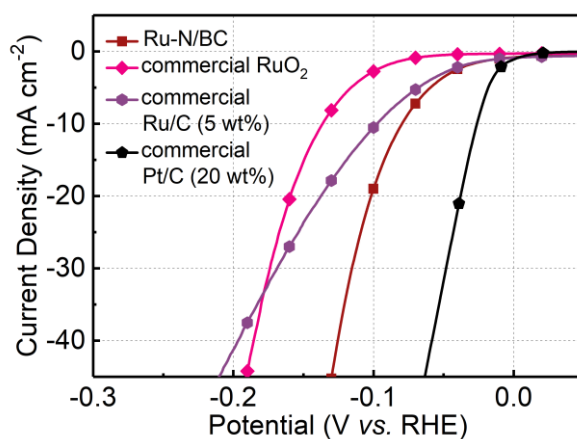

Figure S15. LSV plots of the Ru–N/BC, Ru/BC, Ru–N/C, Ru/C, commercial RuO_2, commercial Ru/C (5 wt.%) and commercial Pt/C (20 wt.%) electrodes in N_2-saturated 0.5 M H_2SO_4 solution at a sweep rate of 5 mV s^{-1}.
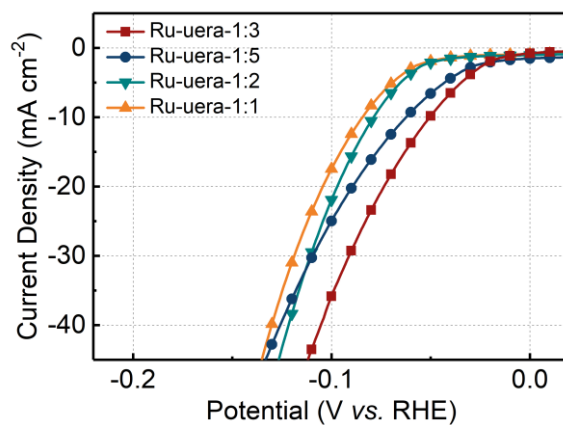
Figure S16. LSV plots of different molar ratio of Ru and urea ligands in Ru–N/BC electrodes in N_2-saturated 1 M KOH solution at a sweep rate of 5 mV s^{-1}.
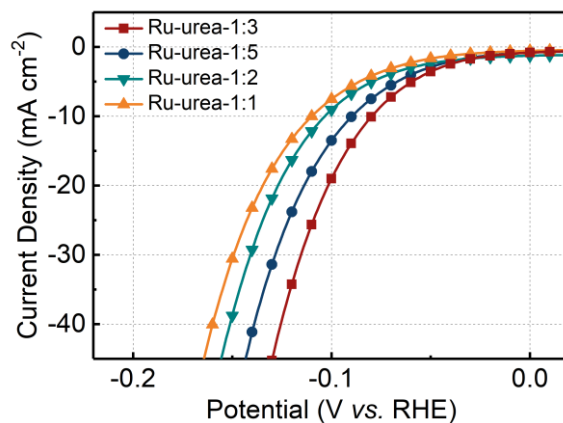

Figure S17. LSV plots of different molar ratio of Ru and urea ligands in Ru–N/BC electrodes in N_2-saturated 0.5 M H_2SO_4 solution at a sweep rate of 5 mV s^{-1}.

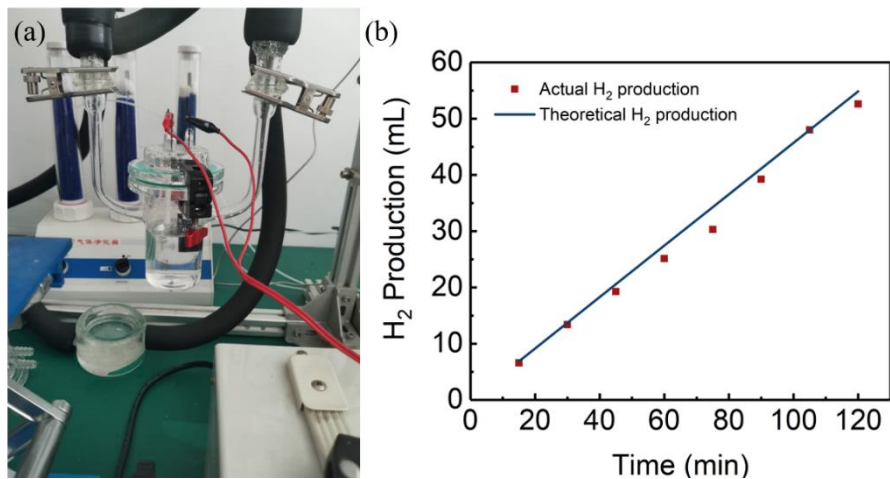Moreover, the effects of the different ligands and metal molar ratio were also considered.

Figure S18. (a) Electrochemistry – gas chromatography in-situ measurement. (b) Actual and theoretical hydrogen production of Ru–N/BC in 0.5 M H_2SO_4 solution.
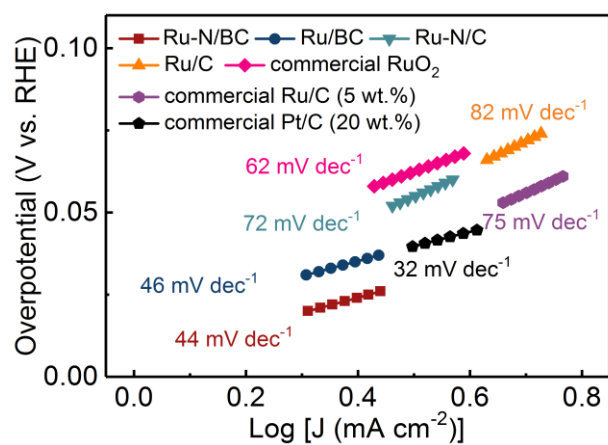

Figure S19. Tafel plots of the Ru–N/BC, Ru/BC, Ru–N/C, Ru/C, commercial RuO_2, commercial Ru/C (5 wt.%) and commercial Pt/C (20 wt.%) electrodes in N_2-saturated 1 M KOH solution at a sweep rate of 5 mV s^{-1}.
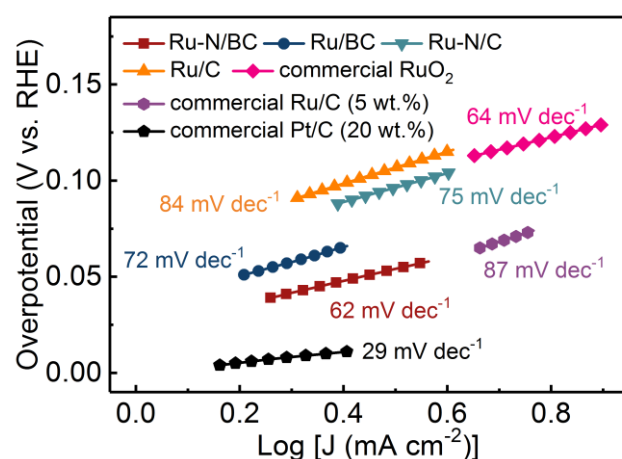
Figure S20. Tafel plots of the Ru–N/BC, Ru/BC, Ru–N/C, Ru/C, commercial RuO₂, commercial Ru/C (5 wt.%) and commercial Pt/C (20 wt.%) electrodes in N₂-saturated 0.5 M H₂SO₄ solution at a sweep rate of 5 mV s⁻¹.
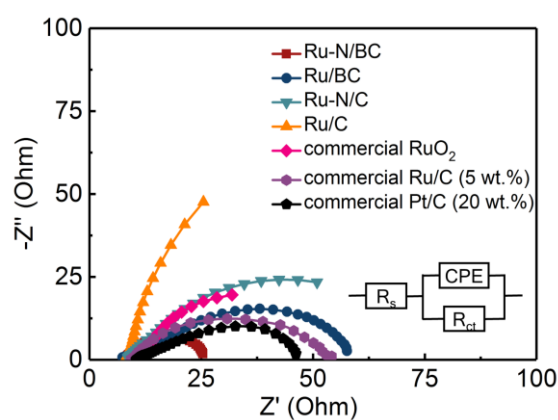

Figure S21. The Nyquist plots of the Ru–N/BC, Ru/BC, Ru–N/C, Ru/C, commercial RuO₂, commercial Ru/C (5 wt.%) and commercial Pt/C (20 wt.%) electrodes at open circuit potential in N₂-saturated 1 M KOH solution. Inset is the equivalent circuit, in which R_s is uncompensated resistance, R_{ct} is charge transfer resistance, and CPE is constant phase element (equivalent to the double-layer capacitance).

Figure S22. The Nyquist plots of the Ru–N/BC, Ru/BC, Ru–N/C, Ru/C, commercial RuO_2 commercial Ru/C (5 wt.%) and commercial Pt/C (20 wt.%) electrodes at open circuit potential in N_2-saturated 0.5 M H_2SO_4 solution. Inset is the equivalent circuit, in which R_s is uncompensated resistance, R_{ct} is charge transfer resistance, and CPE is constant phase element (equivalent to the double-layer capacitance).
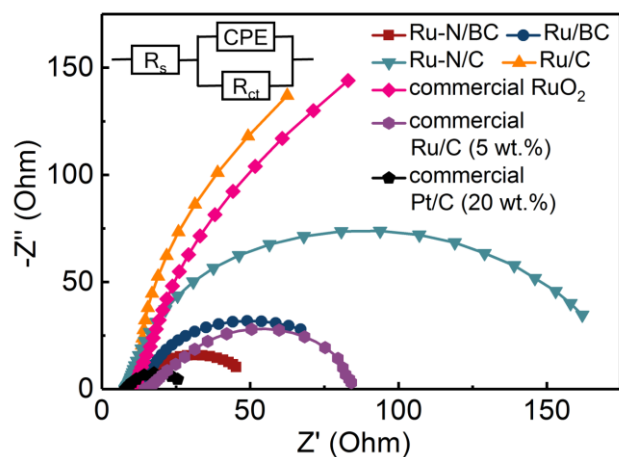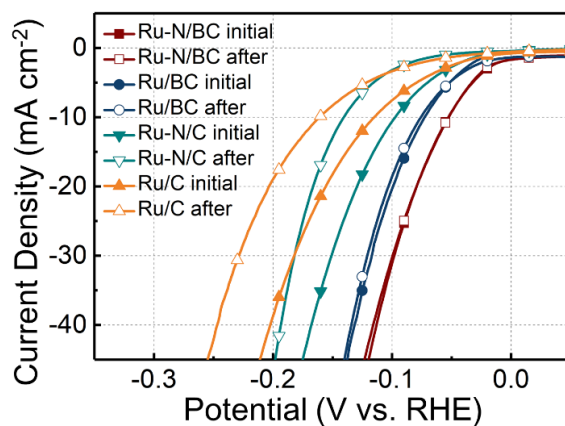

Figure S23. The durability of the Ru–N/BC, Ru/BC, Ru–N/C, Ru/C electrodes for 3000 cycles potential sweeps from 0.2 to -0.1 V in 1M KOH solution.
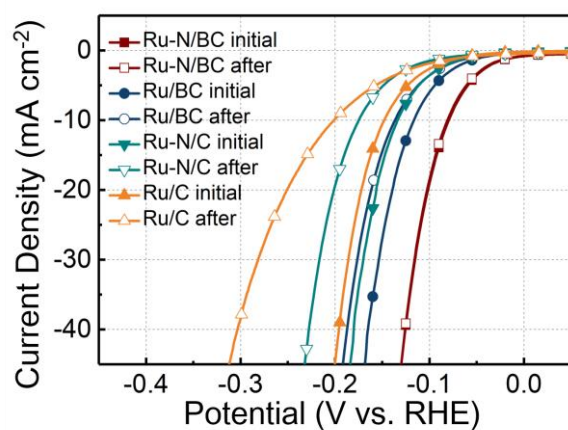
Figure S24. The durability f the Ru–N/BC, Ru/BC, Ru–N/C, Ru/C electrodes for 3000 cycles potential sweeps from 0.2 to -0.1 V in 0.5M H_2SO_4 solution.
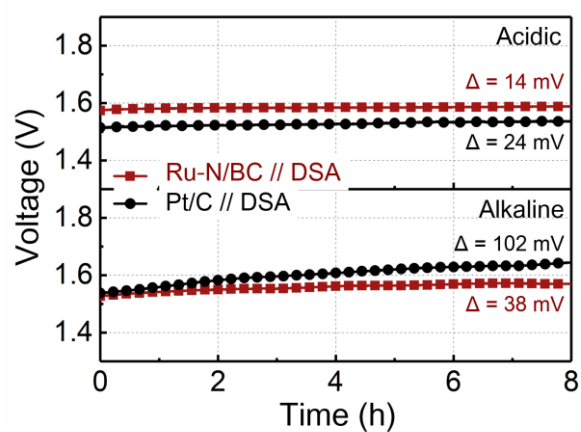
Figure S25. The chronopotentiometry tests of Ru–N/BC and commercial Pt/C in two electrode system with the DSA as the counter electrode in 0.5 M H_2SO_4 and 1 M KOH solutions.
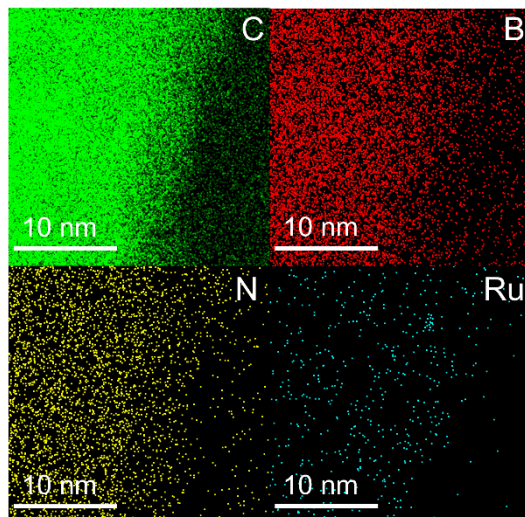
Figure S26 Element distribution mapping images of Ru–N/BC after the chronopotentiometry testing in 0.5 M H_2SO_4 solution.

Figure S27. The normalized Ru *K*-edge XANES spectra of (a) Ru–N/BC, (b) Ru/BC, (c) Ru–N/C and (d) Ru/C before and after the long-term chronopotentiometry testing in 0.5 M H_2SO_4 solution.

Table S9. Comparison of TOFs in alkaline and acidic electrolyte for Ru–N/BC with the reported noble metal baesd and non-noble metal electrocatalysts.
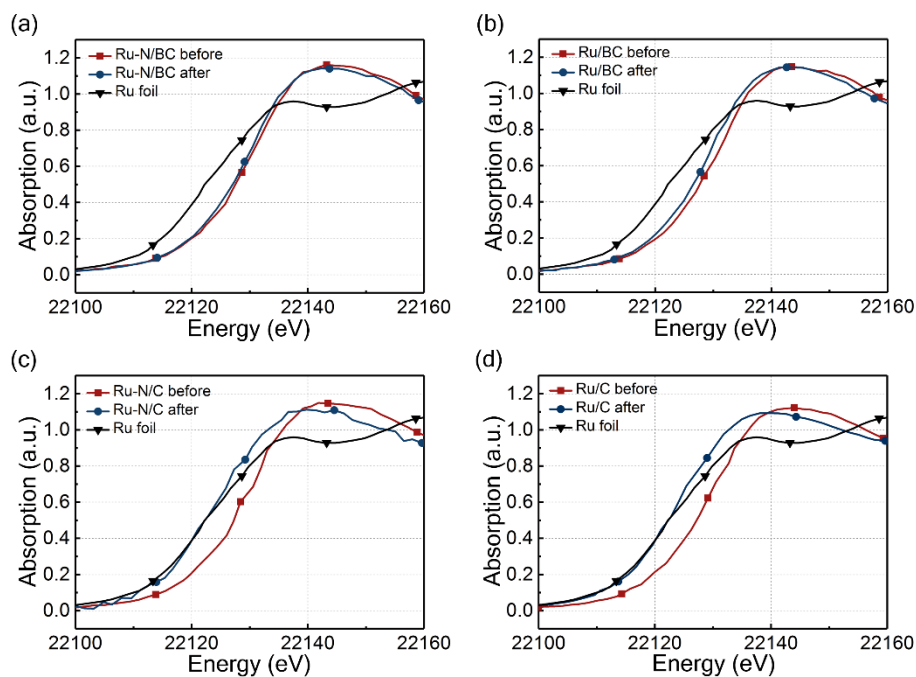
Sample	Electrolyte	TOFs (H_2 s^{-1})	Ref.
Ru@C$_2$N	1M KOH	0.75 H s^{-1} at 50 mV	S1
	0.5 M H_2SO_4	0.67 H s^{-1} at 25 mV	
Ru/NG-750	1 M KOH	0.35 H s^{-1} at 100 mV	S2
	0.5 M H_2SO_4	0.04 H s^{-1} at 100 mV	
Ru/C$_3$N$_4$/C	1 M KOH	4.20 H s^{-1} at 100 mV	S3
Ru@NG	1 M KOH	0.44 H s^{-1} at 50 mV	S4
	0.5 M H_2SO_4	0.25 H s^{-1} at 50 mV	
Ru@GnP	1 M H_2SO_4	2.10 H s^{-1} at 50 mV	S5
Ru@NC	1 M KOH	1.00 H s^{-1} at 25 mV	S6
α-Mo$_2$C	1 M KOH	0.90 H s^{-1} at 200 mV	S7
Mo$_2$N	1 M KOH	0.07 H s^{-1} at 250 mV	
Ni$_5$P$_4$	1 M KOH	0.23 H s^{-1} at 200 mV	S8
Ni-Mo	1 M KOH	0.05 H s^{-1} at 100 mV	S9
UHVMoS$_2$|Au(111)	0.5 M H_2SO_4	1.00 H s^{-1} at 100 mV	S10
RuP/NPC	0.5 M H_2SO_4	0.05 H s^{-1} at 25 mV	S11
Rh$_x$P/NPC	0.5 M H_2SO_4	0.45 H s^{-1} at 25 mV	
CoN$_x$/C	0.5 M H_2SO_4	0.40 H s^{-1} at 100 mV	S12
Co-NG	0.5 M H_2SO_4	0.40 H s^{-1} at 150 mV	S13
CoP	0.5 M H_2SO_4	0.05 H s^{-1} at 100 mV	S14
Mo$_3$S$_{13}$	0.5 M H_2SO_4	0.70 H s^{-1} at 200 mV	S15
Ru–N/BC	1 M KOH	2.82 H s^{-1} at 50 mV	This work
	0.5 M H_2SO_4	1.02 H s^{-1} at 50 mV	

References

S1. Mahmood, J.; Li, F.; Jung, S.-M.; Okyay, M. S.; Ahmad, I.; Kim, S.-J.; Park, N.; Jeong, H. Y.; Baek, J.-B., An efficient and pH-universal ruthenium-based catalyst for the hydrogen evolution reaction. *Nat. Nanotechnol.*, 2017, **12**, 441-446

S2. Ye, R.; Liu, Y.; Peng, Z.; Wang, T.; Jalilov, A. S.; Yakobson, B. I.; Wei, S.-H.; Tour, J. M., High Performance Electrocatalytic Reaction of Hydrogen and Oxygen on Ruthenium Nanoclusters. *ACS Appl. Mater. Inter.*, 2017, **9**, 3785-3791.

S3. Zheng, Y.; Jiao, Y.; Zhu, Y.; Li, L. H.; Han, Y.; Chen, Y.; Jaroniec, M.; Qiao, S.-Z., High Electrocatalytic Hydrogen Evolution Activity of an Anomalous Ruthenium Catalyst. *J. Am. Chem. Soc.*, 2016, **138**, 16174-16181.

S4. Yang, J.; Guo, H.; Chen, S.; Li, Y.; Cai, C.; Gao, P.; Wang, L.; Zhang, Y.; Sun, R.; Niu, X.; Wang, Z., Anchoring and space-confinement effects to form ultrafine Ru nanoclusters for efficient hydrogen generation. *J. Mater. Chem. A*, 2018, **6**, 13859-13866.

S5. Li, F.; Han, G.-F.; Noh, H.-J.; Ahmad, I.; Jeon, I.-Y.; Baek, J.-B., Mechanochemically Assisted Synthesis of a Ru Catalyst for Hydrogen Evolution with Performance Superior to Pt in Both Acidic and Alkaline Media. *Adv. Mater.*, 2018, **30**, 1803676.

S6. Wang, Z.-L.; Sun, K.; Henzie, J.; Hao, X.; Li, C.; Takei, T.; Kang, Y.-M.; Yamauchi, Y., Spatially Confined Assembly of Monodisperse Ruthenium Nanoclusters in a Hierarchically Ordered Carbon Electrode for Efficient Hydrogen Evolution. *Angew. Chem. Int. Edit.*, 2018, **57**, 5848-5852.

S7. Ma, L.; Ting, L. R. L.; Molinari, V.; Giordano, C.; Yeo, B. S., Efficient hydrogen evolution reaction catalyzed by molybdenum carbide and molybdenum nitride nanocatalysts synthesized via the urea glass route. *J. Mater. Chem. A,* 2015, **3**, 8361-8368.

S8. Laursen, A. B.; Patraju, K. R.; Whitaker, M. J.; Retuerto, M.; Sarkar, T.; Yao, N.; Ramanujachary, K. V.; Greenblatt, M.; Dismukes, G. C., Nanocrystalline Ni_5P_4: a hydrogen evolution electrocatalyst of exceptional efficiency in both alkaline and acidic media. *Energy Environ. Sci.*, 2015, **8**, 1027-1034.

S9. McKone, J. R.; Sadtler, B. F.; Werlang, C. A.; Lewis, N. S.; Gray, H. B., Ni–Mo Nanopowders for Efficient Electrochemical Hydrogen Evolution. *ACS Catal.*, 2013, **3**, 166-169.

S10. Jaramillo, T. F.; Jørgensen, K. P.; Bonde, J.; Nielsen, J. H.; Horch, S.; Chorkendorff, I., Identification of Active Edge Sites for Electrochemical H_2 Evolution from MoS_2 Nanocatalysts. *Science*, 2007, **317**, 100-102.

S11. Qin, Q.; Jang, H.; Chen, L.; Nam, G.; Liu, X.; Cho, J., Low Loading of Rh_xP and RuP on N, P Codoped Carbon as Two Trifunctional Electrocatalysts for the Oxygen and Hydrogen Electrode Reactions. *Adv. Energy Mater.,* 2018, **8**, 1801478.

S12. Liang, H.-W.; Brüller, S.; Dong, R.; Zhang, J.; Feng, X.; Müllen, K., Molecular metal–N_x centres in porous carbon for electrocatalytic hydrogen evolution. *Nat. Commun.*, 2015, **6**, 7992.

S13. Fei, H.; Dong, J.; Arellano-Jiménez, M. J.; Ye, G.; Dong Kim, N.; Samuel, E. L. G.; Peng, Z.; Zhu, Z.; Qin, F.; Bao, J.; Yacaman, M. J.; Ajayan, P. M.; Chen, D.; Tour,

J. M., Atomic cobalt on nitrogen-doped graphene for hydrogen generation. *Nat. Commun.*, 2015, **6**, 8668.

S14. Popczun, E. J.; Read, C. G.; Roske, C. W.; Lewis, N. S.; Schaak, R. E., Highly Active Electrocatalysis of the Hydrogen Evolution Reaction by Cobalt Phosphide Nanoparticles. *Angew. Chem. Int. Edit.*, 2014, **53**, 5427-5430.

S15. Kibsgaard, J.; Jaramillo, T. F.; Besenbacher, F., Building an appropriate active-site motif into a hydrogen-evolution catalyst with thiomolybdate $[Mo_3S_{13}]^{2-}$ clusters. *Nat. Chem.*, 2014, **6**, 248-253.